

## Wave Packet Dynamics in Synthetic Non-Abelian Gauge Fields

Mehedi Hasan<sup>1,2,\*</sup> Chetan Sriram Madasu<sup>1,2</sup> Ketan D. Rathod,<sup>3,2,†</sup> Chang Chi Kwong<sup>1,2</sup>  
 Christian Miniatura<sup>1,2,3,4,1,5</sup> Frédéric Chevy<sup>6</sup> and David Wilkowski<sup>1,2,3,‡</sup>

<sup>1</sup>*Nanyang Quantum Hub, School of Physical and Mathematical Sciences, Nanyang Technological University, 21 Nanyang Link, Singapore 637371, Singapore*


<sup>2</sup>*MajuLab, International Joint Research Unit IRL 3654, CNRS, Université Côte d'Azur, Sorbonne Université, National University of Singapore, Nanyang Technological University, Singapore*

<sup>3</sup>*Centre for Quantum Technologies, National University of Singapore, 117543 Singapore, Singapore*

<sup>4</sup>*Department of Physics, National University of Singapore, 2 Science Drive 3, Singapore 117542, Singapore*

<sup>5</sup>*Université Côte d'Azur, CNRS, INPHYNI, 06108 Nice, France*

<sup>6</sup>*Laboratoire de Physique de l'École normale supérieure, ENS, Université PSL, CNRS, Sorbonne Université, Université de Paris, F-75005 Paris, France*

 (Received 14 February 2022; revised 10 April 2022; accepted 29 July 2022; published 19 September 2022)

It is generally admitted that in quantum mechanics, the electromagnetic potentials have physical interpretations otherwise absent in classical physics as illustrated by the Aharonov-Bohm effect. In 1984, Berry interpreted this effect as a geometrical phase factor. The same year, Wilczek and Zee generalized the concept of Berry phases to degenerate levels and showed that a non-Abelian gauge field arises in these systems. In sharp contrast with the Abelian case, spatially uniform non-Abelian gauge fields can induce particle noninertial motion. We explore this intriguing phenomenon with a degenerated Fermionic atomic gas subject to a two-dimensional synthetic SU(2) non-Abelian gauge field. We reveal the spin Hall nature of the noninertial dynamic as well as its anisotropy in amplitude and frequency due to the spin texture of the system. We finally draw the similarities and differences of the observed wave packet dynamic and the celebrated *Zitterbewegung* effect of the relativistic Dirac equation.

DOI: 10.1103/PhysRevLett.129.130402

Since the pioneering work of Lin and co-workers on synthetic magnetic fields [1], intensive works on quantum simulators such as ultracold-gas platforms [2–7] or photonic circuits [8] have been carried out to generate and explore artificial Abelian or non-Abelian gauge fields. The overarching objective is to explore geometrical and topological properties of quantum matter and materials. In particular, thanks to the noncommutative nature of the components of non-Abelian gauge fields, the eigenstates of the Hamiltonian are characterized by a momentum-dependent spin texture that leads to a myriad of phenomena such as spin phase separations [9,10], topological Lifshitz transitions in a degenerate Fermi gas [11], topological phases in a Bose-Einstein condensate [12], or the Josephson-like effect for interacting quantum gases [13]. The band structure, the spin texture, and the topology properties of two-dimensional (2D) spin-orbit coupled ultracold-atom systems have been reported in [14–16].

The coupling to a non-Abelian gauge field can take the form of a spin-orbit coupling (SOC) Hamiltonian [2],

$$\hat{H}_{\text{SOC}} = -\hat{\mathbf{p}} \cdot \hat{\mathbf{A}}/m, \quad (1)$$

where  $\hat{\mathbf{p}}$  is the momentum operator of the particle,  $m$  its mass, and  $\hat{\mathbf{A}}$  the non-Abelian gauge field operator acting in the

pseudospin space. For systems under SU(2) symmetry, the wave packet dynamics of a SOC system is predicted to exhibit an oscillatory behavior, similar to the *Zitterbewegung* of the Dirac equation, i.e., a trembling motion of a particle associated with a quantum Rabi flopping of the pseudospin [17–24]. The oscillatory behavior of the wave packet has been experimentally studied in one-dimensional (1D) systems, where the SOC term reduces to a single component gauge field [25–28]. In this context, it has been shown that the *Zitterbewegung* is present if the total Hamiltonian includes a scalar potential, which does not commute with the SOC Hamiltonian [26]. In the Dirac equation the scalar term is the mass operator of the particle-antiparticle system. In the 1D SOC Hamiltonians experimentally explored in photonic platforms [25], trapped ions [26], and ultracold gases [27,28], the scalar potential is a Zeeman-like term.

In this Letter, we report on studies of the atomic wave packet dynamics in a two-dimensional (2D) spatially uniform SU(2) non-Abelian gauge field. As a key feature, the wave packet shows oscillatory dynamics coming from the SOC Hamiltonian only, i.e., without any scalar potentials. The occurrence of the dynamics can be understood by deriving the time evolution of the velocity operator  $\hat{\mathbf{v}} = (\hat{\mathbf{p}} - \hat{\mathbf{A}})/m$  in the Heisenberg picture. It leads to a non-inertial force depending on the particle momentum,

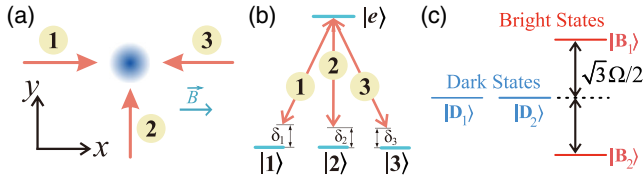


FIG. 1. (a) Real-space configuration of the tripod laser beams. The three co-planar beams (red arrows) define the plane ( $Ox, Oy$ ) orthogonal to the gravity pull. A 67 G bias magnetic field, applied along  $Ox$ , allows us to isolate the tripod system among the ( $^1S_0, F_g = 9/2$ )  $\rightarrow$  ( $^3P_1, F_e = 9/2$ ) Zeeman manifold of the intercombination line. Counterpropagating beams 1 and 3 along  $Ox$  have opposite circular polarizations and address  $\sigma_+$  and  $\sigma_-$  transitions, respectively. The orthogonal beam 2 is linearly polarized along  $Ox$  and addresses a  $\pi$  transition. (b) The tripod laser beam  $a$  drives the transition  $|a\rangle \leftrightarrow |e\rangle$  with a detuning  $\delta_a$  ( $a = 1, 2, 3$ ). The resonant Rabi frequencies are all equal to  $\Omega/2\pi = 210$  kHz. (c) The internal dressed-state basis of the system features two degenerate dark states (in blue) uncoupled to the laser beams and two bright states (in red) shifted from the dark states by  $\pm\sqrt{3}\hbar\Omega/2$ .

$$m \frac{d\hat{\mathbf{v}}}{dt} = \frac{im}{\hbar} [\hat{H}_{\text{SOC}}, \hat{\mathbf{v}}] = -\frac{i}{m\hbar} \hat{\mathbf{p}} \times (\hat{\mathbf{A}} \times \hat{\mathbf{A}}). \quad (2)$$

Two important observations can be made from Eq. (2). First, even for an uniform gauge field, the 2D dynamics is strongly affected by the non-Abelian nature of the gauge field since the velocity is no longer constant when  $(\hat{\mathbf{A}} \times \hat{\mathbf{A}})$  is nonzero. Second, since the velocity component along the momentum does not change in time, the nontrivial wave packet dynamics occurs in the plane transverse to the momentum. This locking of the dynamics at right angle of the momentum is reminiscent of the spin Hall effect [29,30]. Note that  $\hat{\mathbf{p}}$  commutes with  $\hat{H}_{\text{SOC}}$  for spatially uniform gauge fields and is then a constant of motion. In this case, the plane of oscillations does not change with time. Another striking feature that we will demonstrate later is the anisotropy of the wave packet dynamic in momentum space induced by the spin texture of the non-Abelian Hamiltonian.

To generate our artificial non-Abelian gauge field, we use three quasis resonant, suitably polarized, laser beams; see Fig. 1(a). These lasers operate on the ( $^1S_0, F_g = 9/2$ )  $\rightarrow$  ( $^3P_1, F_e = 9/2$ ) intercombination line at 689 nm (frequency linewidth  $\Gamma/2\pi = 7.5$  kHz) of the fermionic strontium isotope  $^{87}\text{Sr}$ . They couple, in a tripod configuration, three Zeeman bare ground states  $|a\rangle \equiv |F_g, m_F\rangle$ , with  $a = 1, 2, 3$  and  $m_F = 5/2, 7/2, 9/2$ , respectively, to the same excited state  $|e\rangle \equiv |F_e, m_F = 7/2\rangle$  and with equal Rabi frequencies  $\Omega/2\pi = 210$  kHz, see Fig. 1(b) [31]. A bias magnetic field of 67 G along the  $x$  axis ensures that the states outside the tripod remain spectators (the Zeeman frequency shift of the excited state is around 7 MHz  $\gg \Omega/2\pi, \Gamma/2\pi$  [32]).

In the dressed-state picture, the internal Hamiltonian of the tripod system has two bright states, coupled to the laser fields, separated by  $\pm\sqrt{3}\hbar\Omega/2$  from two degenerate zero-energy dark states, see Fig. 1(c). The bright or dark state energy separation being large enough, the quantum state of the atoms remains and evolves in time in the dark state manifold [31]. The dark states representation in the bare-state basis reads

$$|D_1\rangle = \frac{1}{\sqrt{2}} (e^{-2ikx}|1\rangle - e^{-ik(x+y)}|2\rangle), \quad (3)$$

$$|D_2\rangle = \frac{1}{\sqrt{6}} (e^{-2ikx}|1\rangle + e^{-ik(x+y)}|2\rangle - 2|3\rangle), \quad (4)$$

where  $k$  is the tripod beams wave number.

For resonant excitation ( $\delta_a = 0$ ), the Hamiltonian in the 2D dark-state manifold takes the form [2]

$$\hat{H}_0 = \frac{(\hat{\mathbf{p}} - \hat{\mathbf{A}})^2}{2m} + \hat{\Phi}. \quad (5)$$

In the pseudospin representation of the dark-state manifold, the vector and scalar gauge field potentials  $(\hat{\mathbf{A}}, \hat{\Phi})$  are represented by  $2 \times 2$  matrices with entries  $\hat{A}_{jk} = i\hbar \langle D_j | \nabla D_k \rangle$  and  $\hat{\Phi}_{jk} = [\hbar^2 \langle \nabla D_j | \nabla D_k \rangle - (\hat{\mathbf{A}}^2)_{jk}] / 2m$  ( $j, k = 1, 2$ ) [2,33].

For quasis resonant excitation ( $|\delta_a| \ll \Omega$ ), the laser detuning contribution in the dark-state manifold reduces to an additional scalar matrix potential. We use it for two crucial purposes: to cancel the scalar term  $\hat{\mathbf{A}}^2/2m + \hat{\Phi}$  obtained by expanding the square in Eq. (5), and to perform a Galilean transformation into an inertial frame moving at an arbitrary velocity  $-\mathbf{v}_0$  by adding a new term  $-\mathbf{v}_0 \cdot \hat{\mathbf{A}}$  (see Sec. C in the Supplemental Material [33]). In this moving frame, and up to inessential constant terms proportional to unity, the Hamiltonian becomes

$$\hat{H} = \frac{\hat{\mathbf{q}}^2}{2m} - \frac{\hat{\mathbf{q}} \cdot \hat{\mathbf{A}}}{m}, \quad (6)$$

where  $\hat{\mathbf{q}} = \hat{\mathbf{p}} + m\mathbf{v}_0$ . We get the expected SOC Hamiltonian without scalar contribution to explore the 2D dynamical properties of this system. Note that the noninertial dynamic is not affected by the discarded spin-independent  $\hat{\mathbf{q}}^2/(2m)$  term [17].

We simulate the Hamiltonian of Eq. (6) using a degenerate Fermi gas at a temperature  $T = 30(3)$  nK, with  $T/T_F = 0.21(4)$ , where  $T_F \approx 143$  nK is the Fermi temperature of our gas. After the cooling and preparation sequences, the atoms are in the state  $|3\rangle$  [33]. We switch on the tripod beams to transfer adiabatically all atoms from state  $|3\rangle$  to one state in the dark-state manifold. For  $v_0 = |\mathbf{v}_0| = 0$ , we expect to populate the dark state  $|D_2\rangle$  [33]. To assess the quality of the adiabatic transfer, we

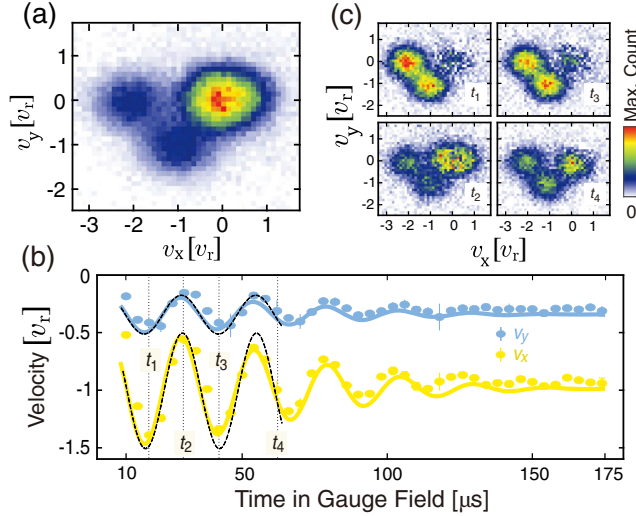


FIG. 2. (a) Time-of-flight fluorescence image recorded at  $v_0 = 0$  after the system has been initialized in the dark state  $|D_2\rangle$ . The ballistic time is 9 ms. As expected from Eq. (4), the measured velocity distribution shows three peaks centered at  $\mathbf{v} = 0$ ,  $\mathbf{v} = -v_r(\hat{\mathbf{e}}_x + \hat{\mathbf{e}}_y)$ , and  $\mathbf{v} = -2v_r\hat{\mathbf{e}}_x$  ( $v_r = \hbar k/m$  is the recoil velocity). These peaks correspond to states  $|3\rangle$ ,  $|2\rangle$ , and  $|1\rangle$ , respectively. (b) Temporal oscillations of the Cartesian coordinates of the averaged velocity obtained for a boost velocity ( $v_0 = 4\sqrt{2}v_r, \theta_0 = 0.6\pi$ ). The solid lines are obtained by numerically integrating the time evolution of the system in the gauge field, initialized in  $|3\rangle$ . We include the  $10 \mu\text{s}$  ramping stage of the tripod beams and finite momentum distribution of our fermionic gas at  $T = 30(3) \text{ nK} = 0.21(4)T_F$ . The dashed lines correspond to the plane-wave model given by Eq. (7) at  $\mathbf{q} = m\mathbf{v}_0$ . Conveniently the time origin is shifted to match the phase oscillations with experimental signal. This time shift is justified inasmuch as Eq. (7) does not incorporate the effect of the laser ramping stage. Its value of about  $5 \mu\text{s}$  is essentially half the ramping duration. (c) Time-of-flight fluorescence images at times  $t_1 = 18, t_2 = 30, t_3 = 42$ , and  $t_4 = 62 \mu\text{s}$ . These times are indicated by vertical dotted lines in (b).

abruptly switch off the tripod beams, let the atoms fall for 9 ms, record the fluorescence image of the gas that we use for a direct measurement of the velocity distribution. As expected from Eq. (4), we observe one velocity peak centered at  $-2v_r\hat{\mathbf{e}}_x$  for state  $|1\rangle$ , a second one at  $-v_r(\hat{\mathbf{e}}_x + \hat{\mathbf{e}}_y)$  for state  $|2\rangle$ , and a third one at the origin for state  $|3\rangle$ ; see Fig. 2(a). By fitting each peak by a Gaussian distribution, we measure the populations  $P_a$ , which agree at a 98% level with the expected values (1/6, 1/6, and 2/3) inferred from Eq. (4). We also checked, by adiabatically switching off the tripod lasers, that 95% of the population returns back to state  $|3\rangle$ . This result indicates a good control of the quantum coherence during the state preparation [33].

With the tripod laser detunings, we now fix a certain mean velocity  $\mathbf{v}_0$  of the ultracold gas in the moving frame that we characterize by its polar coordinates  $(v_0, \theta_0)$  in the tripod laser plane. We let the system evolve in the gauge fields for a time  $t$  and measure the bare state populations

$P_a(t)$  by the time-of-flight (TOF) technique. The experimentally inferred momentum-averaged velocity in the laboratory frame is simply  $\mathbf{v}_{\text{exp}}(t) = -v_r[(2P_1 + P_2)\hat{\mathbf{e}}_x + P_2\hat{\mathbf{e}}_y]$ . The observed temporal oscillations of the velocity, along the  $x$  and  $y$  axis, are shown in Fig. 2(b) for  $v_0 = 4\sqrt{2}v_r$  and  $\theta_0 = 0.6\pi$ . They constitute the first experimental observation of the noninertial wave packet motion induced by a 2D bulk non-Abelian gauge field on an ultracold gas, without scalar potentials. The damping of the oscillations is due to the finite momentum dispersion  $\delta p \sim 0.4\hbar k$  of our degenerate Fermi gas. The solid line in Fig. 2(b) is the theoretical prediction obtained without any fitting parameters by numerically integrating the velocity operator evolutions in the Heisenberg picture, including the finite ramping sequence of the tripod beams, and averaging over the initial momentum distribution [33]. The dashed lines in Fig. 2(b) are the theoretical predictions for a wave packet in the gauge fields without any laser ramping stage in the dark state  $|D_2\rangle$  and with well-defined momentum  $\mathbf{q} = m\mathbf{v}_0$ . The mean velocity in the laboratory frame of this plane-wave model reads [17]

$$\mathbf{v}(t) = v_r\mathbf{u}_1(\theta_0) + v_rf(\theta_0)\cos\omega t\hat{\mathbf{e}}_{\theta_0}, \quad (7)$$

where the last term captures the noninertial effect with

$$f(\theta_0) = \frac{\cos\theta_0 - \sin\theta_0}{2(2 + \cos 2\theta_0)}, \quad (8)$$

and

$$\omega = \frac{2kv_0}{3}\sqrt{2 + \cos 2\theta_0}. \quad (9)$$

The complete derivation of Eqs. (7)–(9) and the expression for  $\mathbf{u}_1(\theta_0)$  can be found in Ref. [33]. As shown in Fig. 2(b), when the boost momentum  $m\mathbf{v}_0$  is large compared to the momentum dispersion of the gas,  $\delta p \ll m\mathbf{v}_0$ , the oscillatory motion at short time is well captured by the plane-wave model, whereas its amplitude is slightly overestimated because of the finite ramping time in the experiment [33]. We will now confront our experimental data to the plane-wave model only.

The other central results of this Letter are the observation of the spin-Hall nature and anisotropy of the 2D motion in momentum space. For this purpose, we vary the mean momentum of the gas in the moving frame via the tripod laser detunings [33]. We will now discuss these phenomena in detail. At first, we recall that Eqs. (2) and (7) indicate that the oscillation motion is a manifestation of a spin Hall effect. As such, the velocity oscillation is locked along a direction perpendicular to the momentum  $\mathbf{q}$ , as it is shown in Fig. 3(a) for  $v_0 = 4\sqrt{2}v_r$ . Here, for each value of  $\theta_0$ , we measure the Cartesian coordinates of the oscillating component of the velocity and extract the

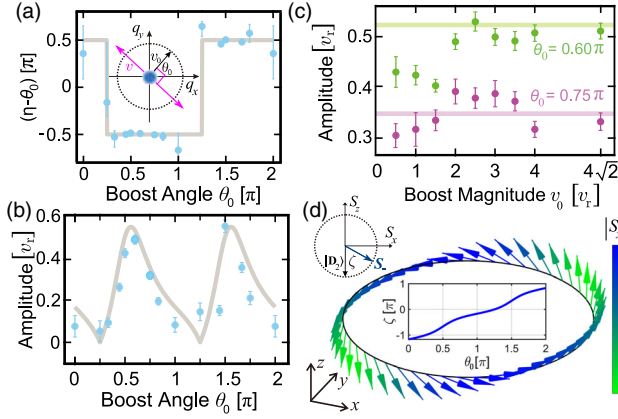


FIG. 3. Direction and amplitude of the wave packet oscillation and spin texture. (a) The oscillatory velocity direction  $\eta$  as function of  $\theta_0$ . The blue points are the experimental data whereas the grey plain curve represents the plane-wave model prediction. The inset shows the direction locking of the oscillation at  $\eta = \theta_0 \pm \pi/2$ . (b) Velocity oscillation amplitude as a function of the boost velocity polar angle  $\theta_0$  for  $v_0 = 4\sqrt{2}v_r$  (points). The solid gray line is the plane-wave prediction  $|f(\theta_0)|$  of Eq. (8). (c) Velocity oscillation amplitude as a function of  $v_0$  at angles  $\theta_0 = 0.6\pi$  (green points) and  $\theta_0 = 0.75\pi$  (magenta points). The green and magenta solid lines are the theoretical predictions from the plane-wave model. The data points in (a), (b), and (c) are obtained with a damped-sinusoidal fit function representing the time evolution of the mean velocity of the atoms [see example in Fig. 2(b)]. All error bars represent 1 standard deviation of uncertainty. (d) Spin texture  $\mathbf{S}$  of the lower energy branch (arrows), Eq. (10), along a circle in the  $(Ox, Oy)$  momentum plane centered at the Dirac point. The spin orientation lies in the  $(Ox, Oz)$  plane, and the color code corresponds to the amplitude of the  $S_x$  component. The central inset shows the evolution of the angle  $\zeta$  of the spin texture in a Bloch sphere representation as a function of  $\theta_0$ . The angle  $\zeta$  is defined with respect to the initial spin orientation  $\langle D_2 | \hat{\sigma} | D_2 \rangle$ ; see example on the top-left inset, where  $\theta_0 = 3\pi/2$  and  $\zeta = \pi/3$ .

direction of the motion. We note that the velocity oscillation flips orientation at  $\theta_0 = \pi/4$  and  $\theta_0 = 5\pi/4$ . As we will see below, the amplitude vanishes at these angles. The gray curve is the theoretical prediction from the plane-wave model.

From the Cartesian coordinates of the velocities, we compute the norm and extract the oscillation amplitude as a function of  $\theta_0$  that we compare to  $v_r |f(\theta_0)|$  as shown in Fig. 3(b) for  $v_0 = 4\sqrt{2}v_r$ . Figure 3(c) shows how the velocity amplitude varies with the boost amplitude  $v_0$  for two fixed values of  $\theta_0$ . When  $mv_0$  is no longer significantly larger than  $\delta p$ , finite momentum dispersion effects kick in and the amplitude departs from the plane-wave model predictions.

To understand the physical origin of the momentum dependence of the velocity oscillations, we derive the local spin textures  $\mathbf{S}_{\pm}(\theta_0) = \langle \varphi_{\pm} | \hat{\sigma} | \varphi_{\pm} \rangle = \mp \mathbf{S}$ , associated to the

upper- and lower-energy eigenstates  $|\varphi_{\pm}\rangle$  of the SOC Hamiltonian. We have [33]

$$S_x = \frac{\sqrt{3}(\cos\theta_0 - \sin\theta_0)}{2\sqrt{2 + \cos 2\theta_0}}, \quad S_z = \frac{(3\cos\theta_0 + \sin\theta_0)}{2\sqrt{2 + \cos 2\theta_0}}, \quad (10)$$

and  $S_y = 0$ . In Fig. 3(d), we show the 3D representation spin texture  $\mathbf{S}_-$  of the lower-energy branch. In the pseudospin language, the initial state  $|D_2\rangle$  of our system is the lower spin state. For  $\theta_0 = \pi/4$  and  $\theta_0 = 5\pi/4$ , the spin textures are along  $Oz$  since  $S_x = 0$  and the initial state  $|D_2\rangle$  identifies with  $|\varphi_-\rangle$  and  $|\varphi_+\rangle$ , respectively [light green arrows in Fig. 3(d)]. As such, Rabi flopping of the pseudospin cannot occur and the oscillations are suppressed. At these angles, the off-diagonal components of the SOC Hamiltonian vanish. In contrast, when  $\tan\theta_0 = -3$ , so at angles  $\theta_0 \approx 0.6\pi$  and  $\theta_0 \approx 1.6\pi$ ,  $S_z = 0$  and the spin textures are along  $Ox$  [blue arrows in Fig. 3(d)]. At these angles the diagonal terms of the SOC Hamiltonian are equal, which corresponds to a resonant excitation in the context of two-level systems. In this case,  $|D_2\rangle$  has equal weights on  $|\varphi_{\pm}\rangle$  and the oscillation is large though not the largest possible because of the  $\theta_0$  dependence in the denominator of  $f(\theta_0)$ .

It is known that a Dirac point is characterized by a winding number that can take two values  $\pm 1$  [40]. From the plane-wave model, this topological number reads  $W = (2\pi)^{-1} \oint (\mathbf{S} \times \nabla_{\theta_0} \mathbf{S})_y d\theta_0 = 1$ . Seen as a mapping from a circle ( $\theta_0$  angle) to another circle (angle  $\zeta$  of  $\mathbf{S}$ ), this reflects the homotopy group of the circle  $\pi_1(S^1) = \mathbb{Z}$  [see insets in Fig. 3(d)]. It indicates that a spin texture  $\mathbf{S}$  is found along a given direction only twice when  $\theta_0$  is circled around  $2\pi$ . In particular, this given direction can be the initial spin orientation  $\langle D_2 | \hat{\sigma} | D_2 \rangle$ , explaining why the oscillation amplitude should vanish at least 2 times along a general loop encircling the Dirac point.

The angular frequency  $\omega \propto kv_0$ , see Eq. (9) quantifies the energy difference between the upper- and lower-energy branches of the Hamiltonian [17]. By varying the boost velocity  $v_0$ , the oscillation can be tuned to a suitable frequency scale where it can be easily detected, for example, in the kHz range as shown in Fig. 2(b). The linear  $v_0$  dependence at fixed  $\theta_0$ , predicted by Eq. (9), is shown in Fig. 4(a). Keeping now  $v_0$  fixed and circling  $\theta_0$  around  $2\pi$ , the trigonometric variation in Eq. (9) is well reproduced; see Fig. 4(b).

In conclusion, we have reported on the first experimental observation of a 2D noninertial dynamics in an ultracold atomic gas subject to a non-Abelian  $SU(2)$  gauge field. This result is consistent with predictions of Refs. [18,19]. We have analyzed in detail the anisotropy of the wave packet motion in momentum space, relating it to a spin-Hall effect. The oscillatory behavior is caused by an interference effect between two spin eigenvalues with different velocities. In a similar way, Schrödinger has interpreted the *Zitterbewegung* as interference occurring between the

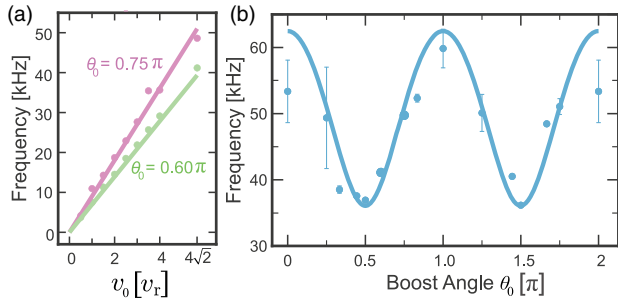


FIG. 4. Oscillation frequency. (a) Variation of the oscillation frequency as a function of the magnitude  $v_0$  of the boost velocity at fixed angles ( $\theta_0 = 0.60\pi$  for the green data points and  $\theta_0 = 0.75\pi$  for the magenta data points) (b) Angular variations of the frequency observed at  $v_0 = 4\sqrt{2}v_r$ . The solid lines in (b) and (c) are the theoretical predictions inferred from the plane-wave model given by Eq. (9). The error bars are 1 standard deviation of uncertainty.

positive and negative energy of a relativistic particle [41]. In both cases, the oscillation roots in the presence of two noncommuting terms in the Hamiltonian. For the 1D *Zitterbewegung* effect, the mass term does not commute with the spin-orbit component, whereas for the 2D non-Abelian gauge field, the noncommutation occurs between the two spin-orbit components.

Our scheme can be extended to  $SU(N)$  systems with  $N > 2$  [42]. There, we expect several oscillation frequencies to enter the noninertial dynamics as the different energy branches will not be necessarily equally spaced. Very generally, the oscillatory motion would measure the energy differences between these different branches and can develop into a powerful spectroscopic tool to map the energy-branch diagram of such multi-level systems [43], in alternative to other existing methods such as rf spectroscopy [15,16,44], Bloch oscillation [45,46], and Fourier transform spectroscopy [47–50]. One could even think of performing selective excitation among energy branches by a clever choice of initial states. Finally, the exact nature of noninertial motion in the presence of dynamic gauge fields seems a promising avenue to explore in the future [51,52].

M. H. thanks Ulrich Schneider and Bo Song for fruitful discussion. This work was supported by the CQT/MoE funding Grant No. R-710-002-016-271, and the Singapore Ministry of Education Academic Research Fund Tier1 Grant No. MOE2018-T1-001-027 and Tier2 Grant No. MOE-T2EP50220-0008.

\*Cavendish Laboratory, University of Cambridge, Cambridge CB3 0HE, United Kingdom.

†Bennett University, Greater Noida 201310, India.

‡david.wilkowski@ntu.edu.sg

[1] Y.-J. Lin, Rob L. Compton, Karina Jiménez-García, James V. Porto, and Ian B. Spielman, Synthetic magnetic

fields for ultracold neutral atoms, *Nature (London)* **462**, 628 (2009).

- [2] Jean Dalibard, Fabrice Gerbier, Gediminas Juzeliūnas, and Patrik Öhberg, Colloquium: Artificial gauge potentials for neutral atoms, *Rev. Mod. Phys.* **83**, 1523 (2011).
- [3] Marcos Atala, Monika Aidelsburger, Julio T Barreiro, Dmitry Abanin, Takuya Kitagawa, Eugene Demler, and Immanuel Bloch, Direct measurement of the zak phase in topological bloch bands, *Nat. Phys.* **9**, 795 (2013).
- [4] Nathan Goldman, G. Juzeliūnas, Patrik Öhberg, and Ian B. Spielman, Light-induced gauge fields for ultracold atoms, *Rep. Prog. Phys.* **77**, 126401 (2014).
- [5] Hui Zhai, Degenerate quantum gases with spin–orbit coupling: A review, *Rep. Prog. Phys.* **78**, 026001 (2015).
- [6] Shanchao Zhang and Gyu-Boong Jo, Recent advances in spin-orbit coupled quantum gases, *J. Phys. Chem. Solids* **128**, 75 (2019).
- [7] N. R. Cooper, J. Dalibard, and I. B. Spielman, Topological bands for ultracold atoms, *Rev. Mod. Phys.* **91**, 015005 (2019).
- [8] Tomoki Ozawa, Hannah M. Price, Alberto Amo, Nathan Goldman, Mohammad Hafezi, Ling Lu, Mikael C. Rechtsman, David Schuster, Jonathan Simon, Oded Zilberberg, and Iacopo Carusotto, Topological photonics, *Rev. Mod. Phys.* **91**, 015006 (2019).
- [9] Y-J Lin, K Jiménez-García, and Ian B Spielman, Spin–orbit-coupled Bose–Einstein condensates, *Nature (London)* **471**, 83 (2011).
- [10] Bo Song, Chengdong He, Shanchao Zhang, Elnur Hajiyev, Wei Huang, Xiong-Jun Liu, and Gyu-Boong Jo, Spin-orbit-coupled two-electron fermi gases of ytterbium atoms, *Phys. Rev. A* **94**, 061604(R) (2016).
- [11] Pengjun Wang, Zeng-Qiang Yu, Zhengkun Fu, Jiao Miao, Lianghai Huang, Shijie Chai, Hui Zhai, and Jing Zhang, Spin-Orbit Coupled Degenerate Fermi Gases, *Phys. Rev. Lett.* **109**, 095301 (2012).
- [12] Andika Putra, F. Salces-Cárcoba, Yuchen Yue, Seiji Sugawa, and I. B. Spielman, Spatial Coherence of Spin-Orbit-Coupled Bose Gases, *Phys. Rev. Lett.* **124**, 053605 (2020).
- [13] Junpeng Hou, Xi-Wang Luo, Kuei Sun, Thomas Bersano, Vandna Gokhroo, Sean Mossman, Peter Engels, and Chuanwei Zhang, Momentum-Space Josephson Effects, *Phys. Rev. Lett.* **120**, 120401 (2018).
- [14] Zhan Wu, Long Zhang, Wei Sun, Xiao-Tian Xu, Bao-Zong Wang, Si-Cong Ji, Youjin Deng, Shuai Chen, Xiong-Jun Liu, and Jian-Wei Pan, Realization of two-dimensional spin–orbit coupling for Bose–Einstein condensates, *Science* **354**, 83 (2016).
- [15] Lianghai Huang, Zengming Meng, Pengjun Wang, Peng Peng, Shao-Liang Zhang, Liangchao Chen, Donghao Li, Qi Zhou, and Jing Zhang, Experimental realization of two-dimensional synthetic spin–orbit coupling in ultracold fermi gases, *Nat. Phys.* **12**, 540 (2016).
- [16] Zengming Meng, Lianghai Huang, Peng Peng, Donghao Li, Liangchao Chen, Yong Xu, Chuanwei Zhang, Pengjun Wang, and Jing Zhang, Experimental Observation of a Topological Band Gap Opening in Ultracold Fermi Gases with Two-Dimensional Spin-Orbit Coupling, *Phys. Rev. Lett.* **117**, 235304 (2016).

- [17] József Cserti and Gyula Dávid, Unified description of Zitterbewegung for spintronic, graphene, and superconducting systems, *Phys. Rev. B* **74**, 172305 (2006).
- [18] Yi-Cai Zhang, Shu-Wei Song, Chao-Fei Liu, and Wu-Ming Liu, Zitterbewegung effect in spin-orbit-coupled spin-1 ultracold atoms, *Phys. Rev. A* **87**, 023612 (2013).
- [19] J. Y. Vaishnav and Charles W. Clark, Observing Zitterbewegung with Ultracold Atoms, *Phys. Rev. Lett.* **100**, 153002 (2008).
- [20] M Merkl, FE Zimmer, G Juzeliūnas, and P Öhberg, Atomic zitterbewegung, *Europhys. Lett.* **83**, 54002 (2008).
- [21] Qi Zhang, Jiangbin Gong, and CH Oh, Driven Dirac-like equation via mirror oscillation: Controlled cold-atom Zitterbewegung, *Phys. Rev. A* **81**, 023608 (2010).
- [22] Yongping Zhang, Li Mao, and Chuanwei Zhang, Mean-Field Dynamics of Spin-Orbit Coupled Bose-Einstein Condensates, *Phys. Rev. Lett.* **108**, 035302 (2012).
- [23] V. Yu Argonov and D. V. Makarov, Zitterbewegung with spin-orbit coupled ultracold atoms in a fluctuating optical lattice, *J. Phys. B* **49**, 175503 (2016).
- [24] Jean Claude Garreau and Véronique Zehnlé, Simulating Dirac models with ultracold atoms in optical lattices, *Phys. Rev. A* **96**, 043627 (2017).
- [25] Felix Dreisow, Matthias Heinrich, Robert Keil, Andreas Tünnermann, Stefan Nolte, Stefano Longhi, and Alexander Szameit, Classical Simulation of Relativistic Zitterbewegung in Photonic Lattices, *Phys. Rev. Lett.* **105**, 143902 (2010).
- [26] Rene Gerritsma, Gerhard Kirchmair, Florian Zähringer, E. Solano, R. Blatt, and C. F. Roos, Quantum simulation of the Dirac equation, *Nature (London)* **463**, 68 (2010).
- [27] Chunlei Qu, Chris Hamner, Ming Gong, Chuanwei Zhang, and Peter Engels, Observation of Zitterbewegung in a spin-orbit-coupled Bose-Einstein condensate, *Phys. Rev. A* **88**, 021604(R) (2013).
- [28] Lindsay J. LeBlanc, M. C. Beeler, Karina Jimenez-Garcia, Abigail R. Perry, Seiji Sugawa, R. A. Williams, and Ian B. Spielman, Direct observation of Zitterbewegung in a Bose-Einstein condensate, *New J. Phys.* **15**, 073011 (2013).
- [29] Matthew C. Beeler, Ross A. Williams, Karina Jimenez-Garcia, Lindsay J. LeBlanc, Abigail R. Perry, and Ian B. Spielman, The spin hall effect in a quantum gas, *Nature (London)* **498**, 201 (2013).
- [30] Yuichiro K. Kato, Roberto C. Myers, Arthur C. Gossard, and David D. Awschalom, Observation of the spin hall effect in semiconductors, *Science* **306**, 1910 (2004).
- [31] Frédéric Leroux, Kanhaiya Pandey, R Rehbi, Frederic Chevy, Christian Miniatura, Benoît Grémaud, and David Wilkowski, Non-Abelian adiabatic geometric transformations in a cold strontium gas, *Nat. Commun.* **9**, 3580 (2018).
- [32] Martin M. Boyd, Tanya Zelevinsky, Andrew D. Ludlow, Sebastian Blatt, Thomas Zanon-Willette, Seth M. Foreman, and Jun Ye, Nuclear spin effects in optical lattice clocks, *Phys. Rev. A* **76**, 022510 (2007).
- [33] See Supplemental Material at <http://link.aps.org/supplemental/10.1103/PhysRevLett.129.130402>, which includes Refs. [34–39], for experimental detail and the derivation of Eqs. (6)–(10).
- [34] Thierry Chaneliere, Ling He, Robin Kaiser, and David Wilkowski, Three dimensional cooling and trapping with a narrow line, *Eur. Phys. J. D* **46**, 507 (2008).
- [35] Tao Yang, Kanhaiya Pandey, Mysore Srinivas Pramod, Frederic Leroux, Chang Chi Kwong, Elnur Hajiyev, Zhong Yi Chia, Bess Fang, and David Wilkowski, A high flux source of cold strontium atoms, *Eur. Phys. J. D* **69**, 1 (2015).
- [36] B. J. DeSalvo, M. Yan, P. G. Mickelson, Y. N. Martinez de Escobar, and T. C. Killian, Degenerate Fermi Gas of SR 87, *Phys. Rev. Lett.* **105**, 030402 (2010).
- [37] Mehedi Hasan, Dynamics of quantum gas in non-abelian gauge field, Ph.D. Thesis, Nanyang Technological University, 2021, <https://dr.ntu.edu.sg/handle/10356/152148>.
- [38] Wolfgang Ketterle and Martin W. Zwierlein, Making, probing and understanding ultracold fermi gases, *Riv. Nuovo Cimento Soc. Ital. Fis.* **31**, 247 (2008).
- [39] Harvey R. Brown and Peter R. Holland, The Galilean covariance of quantum mechanics in the case of external fields, *Am. J. Phys.* **67**, 204 (1999).
- [40] Gilles Montambaux, Lih-King Lim, Jean-Noël Fuchs, and Frédéric Piéchon, Winding Vector: How to Annihilate Two Dirac Points with the Same Charge, *Phys. Rev. Lett.* **121**, 256402 (2018).
- [41] Erwin Schrödinger, Über die kräftefreie Bewegung in der relativistischen Quantenmechanik, *Sitz. Preuss. Akad. Wiss. Phys.-Math. Kl.* **24**, 418 (1930).
- [42] Yu-Xin Hu, Christian Miniatura, David Wilkowski, and Benoit Grémaud, U(3) artificial gauge fields for cold atoms, *Phys. Rev. A* **90**, 023601 (2014).
- [43] A. Valdés-Curiel, D. Trypogeorgos, Q.-Y. Liang, R. P. Anderson, and I. B. Spielman, Topological features without a lattice in Rashba spin-orbit coupled atoms, *Nat. Commun.* **12**, 593 (2021).
- [44] Lawrence W. Cheuk, Ariel T. Sommer, Zoran Hadzibabic, Tarik Yefsah, Waseem S. Bakr, and Martin W. Zwierlein, Spin-Injection Spectroscopy of a Spin-Orbit Coupled Fermi Gas, *Phys. Rev. Lett.* **109**, 095302 (2012).
- [45] Gregor Jotzu, Michael Messer, Rémi Desbuquois, Martin Lebrat, Thomas Uehlinger, Daniel Greif, and Tilman Esslinger, Experimental realization of the topological Haldane model with ultracold fermions, *Nature (London)* **515**, 237 (2014).
- [46] Tracy Li, Lucia Duca, Martin Reitter, Fabian Grusdt, Eugene Demler, Manuel Endres, Monika Schleier-Smith, Immanuel Bloch, and Ulrich Schneider, Bloch state tomography using wilson lines, *Science* **352**, 1094 (2016).
- [47] A. Valdés-Curiel, D. Trypogeorgos, E. E. Marshall, and I. B. Spielman, Fourier transform spectroscopy of a spin-orbit coupled Bose gas, *New J. Phys.* **19**, 033025 (2017).
- [48] Tracy Li, Lucia Duca, Martin Reitter, Fabian Grusdt, Eugene Demler, Manuel Endres, Monika Schleier-Smith, Immanuel Bloch, and Ulrich Schneider, Bloch state tomography using Wilson lines, *Science* **352**, 1094 (2016).
- [49] L. Duca, T. Li, M. Reitter, I. Bloch, M. Schleier-Smith, and U. Schneider, An Aharonov-Bohm interferometer for determining Bloch band topology, *Science* **347**, 288 (2015).
- [50] Leticia Tarruell, Daniel Greif, Thomas Uehlinger, Gregor Jotzu, and Tilman Esslinger, Creating, moving and merging Dirac points with a fermi gas in a tunable honeycomb lattice, *Nature (London)* **483**, 302 (2012).
- [51] Mari Carmen Bañuls *et al.*, Simulating lattice gauge theories within quantum technologies, *Eur. Phys. J. D* **74**, 165 (2020).
- [52] M. Aidelsburger *et al.*, Cold atoms meet lattice gauge theory, *Phil. Trans. R. Soc. A* **380**, 20210064 (2021).